



CHORUS

This is the accepted manuscript made available via CHORUS. The article has been published as:

Bridging the rheology of granular flows in three regimes

Sebastian Chialvo, Jin Sun, and Sankaran Sundaresan

Phys. Rev. E **85**, 021305 — Published 13 February 2012

DOI: [10.1103/PhysRevE.85.021305](https://doi.org/10.1103/PhysRevE.85.021305)

Bridging the rheology of granular flows in three regimes

Sebastian Chialvo,¹ Jin Sun,² and Sankaran Sundaresan¹

¹*Chemical and Biological Engineering Department,
Princeton University, Princeton, NJ 08540, USA*

²*Institute for Infrastructure and Environment, University of Edinburgh, Edinburgh EH9 3JL, Scotland, UK*

We investigate the rheology of granular materials via molecular dynamics simulations of homogeneous, simple shear flows of soft, frictional, noncohesive spheres. In agreement with previous results for frictionless particles, we observe three flow regimes existing in different domains of particle volume fraction and shear rate, with all stress data collapsing upon scaling by powers of the distance to the jamming point. Though this jamming point is a function of the interparticle friction coefficient, the relation between pressure and strain rate at this point is found to be independent of friction. We also propose a rheological model that blends the asymptotic relations in each regime to obtain a general description for these flows. Finally, we show that departure from inertial number scalings is a direct result of particle softness, with a dimensionless shear rate characterizing the transition.

PACS numbers: 45.70.-n, 47.57.Gc, 64.60.F-, 64.70.ps, 83.10.Gr, 83.80.Fg

I. INTRODUCTION

Flows of granular matter occur in numerous geophysical and industrial processes and, as such, have garnered the attention of researchers for many years. Early efforts to describe these flows focused on either dilute flows (where kinetic theories [1–4] apply and which belong to the *inertial* regime) or very dense, slow flows (or *quasi-static* flows, for which plasticity models [5, 6] can be used). However, attention has turned recently to the interface between these two regimes in the context of a jamming transition, proposed to occur in granular and other soft matter [7]. Of particular interest are several works that find a critical rheology around this transition in flows of frictionless, soft spheres [8–11] and disks [12, 13]. Furthermore, they find scalings for the mean normal and shear stresses with respect to volume fraction that apply over a wide range of volume fractions and shear rates. Granular materials, though, are typically considered stiff, frictional materials, and to date there has been little work on identifying a critical rheology [14, 15] for such matter despite significant progress in understanding their static jamming behavior [16–19]. In this paper, we investigate the rheology of frictional granular matter about the jamming transition and discuss the construction of a rheological model for flows in the quasi-static, inertial, and *intermediate* (i.e. critical) regimes.

II. SIMULATION METHODS

We perform computer simulations using a package of the discrete element method (DEM) [20] implemented in the molecular dynamics package LAMMPS [21]. In DEM, particles interact only via repulsive, finite-range contact forces. We employ a spring-dashpot model, for which the normal and tangential forces on a spherical particle i resulting from the contact of two identical

spheres i and j are

$$\mathbf{F}_{ij}^n = f(\delta/d) [k_n \delta_{ij} \mathbf{n}_{ij} - \gamma_n m_{\text{eff}} \mathbf{v}_{ij}^n] \quad (1)$$

$$\mathbf{F}_{ij}^t = f(\delta/d) [-k_t \mathbf{u}_{ij}^t - \gamma_t m_{\text{eff}} \mathbf{v}_{ij}^t], \quad (2)$$

for overlap distance δ_{ij} , particle diameter d , spring stiffness constants k_n and k_t , viscous damping constants γ_n and γ_t , effective mass $m_{\text{eff}} = m_i m_j / (m_i + m_j)$ for particle masses m_i and m_j , relative particle velocity components \mathbf{v}_{ij}^n and \mathbf{v}_{ij}^t , and elastic shear displacement \mathbf{u}_{ij}^t . A linear spring-dashpot (LSD) model is chosen by setting the function $f(x) = 1$, while a Hertzian model is set by $f(x) = \sqrt{x}$; the LSD model will be used throughout this paper except where noted explicitly. By Newton’s Third Law, particle j experiences the force $\mathbf{F}_{ji} = -\mathbf{F}_{ij}$. Particle sliding occurs when the Coulomb criterion $|\mathbf{F}_{ij}^t| < \mu |\mathbf{F}_{ij}^n|$ is not satisfied for particle friction coefficient μ . Additionally, after setting $k_t/k_n = 2/7$ and $\gamma_t = 0$, we set γ_n such that the restitution coefficient $e = \exp(-\gamma_n \pi / \sqrt{4k_n/m_{\text{eff}} - \gamma_n^2}) = 0.7$ in the LSD case.

Using the above contact model, assemblies of about 2000 particles in a periodic box are subjected to homogeneous steady simple shear at a shear rate $\dot{\gamma}$ via the Lees-Edwards boundary condition [22]. The box size, and hence the solids volume fraction ϕ , are kept constant for each simulation. The macroscopic stress tensor is calculated as

$$\boldsymbol{\sigma} = \frac{1}{V} \sum_i \left[\sum_{j \neq i} \frac{1}{2} \mathbf{r}_{ij} \mathbf{F}_{ij} + m_i (\mathbf{v}'_i) (\mathbf{v}'_i) \right], \quad (3)$$

where V is the box volume, \mathbf{r}_{ij} is the center-to-center contact vector from particle j to particle i , and \mathbf{v}'_i is the particle velocity relative to its mean streaming velocity; from this result, an ensemble-averaged pressure $p = (\sigma_{xx} + \sigma_{yy} + \sigma_{zz})/3$ and shear stress $\tau = \sigma_{xz}$ can be extracted. All macroscopic quantities will be presented in dimensionless form, scaled by some combination of the particle diameter d , stiffness $k = k_n$, and solid density ρ_s . Since particles are assumed to overlap without

TABLE I. Estimates of the critical volume fraction ϕ_c for different cases of the interparticle friction coefficient. The value of ϕ_c for the frictionless case agrees with the experimentally determined result of Nordstrom [10].

μ	0.0	0.1	0.3	0.5	1.0
ϕ_c	0.636	0.613	0.596	0.587	0.581

deformation, we ensure that the average overlap is small (i.e. $\delta/d \approx pd/k \lesssim 0.07$).

III. FLOW REGIMES

We performed a series of simple shear simulations over a range of shear rates and volume fractions reaching into all three flow regimes and for several particle friction coefficients between 0 and 1. Figure 1 shows the scaled pressure pd/k versus the scaled shear rate $\hat{\gamma} = \dot{\gamma}d/\sqrt{k}/(\rho_s d)$ at various volume fractions for (a) $\mu = 0.5$ and (b) $\mu = 0.1$. At low shear rates, there is an observed separatrix occurring at a critical volume fraction ϕ_c , which we identify as the jamming point; stresses scale quadratically with shear rate below ϕ_c but show no rate dependence above it. These two bands correspond to the inertial and quasi-static regimes, respectively. As shear rate increases, the quasi-static and inertial isochores approach a shared asymptote characteristic of the critical point in which dependence on the volume fraction vanishes; this region corresponds to the intermediate regime. Interestingly, the intermediate asymptote appears to be independent of the friction coefficient, in contrast to results at lower shear rates and despite the fact that $\phi_c = \phi_c(\mu)$. Values of ϕ_c for different cases of μ are presented in Table I. It should be noted that these critical values inferred from dynamical behavior of sheared systems are unique for each case of μ and hence may differ from the jamming points of static packings, which are not unique and depend on the compactivity [17].

A better understanding of the regime transitions can be gained by constructing a regime map, or “phase diagram,” from the slopes of the curves in Figure 1. Such a map is shown in Figure 2. The intermediate regime is observed to lie in a window centered around $\phi = \phi_c$, and the width of this window is dependent on the value of the dimensionless shear rate. This feature has important implications for the modeling of dense granular flows. The large stiffness of granular materials such as sand or glass beads has been used to justify the modeling of granular particles as (infinitely) hard spheres. For such particles, dimensional analysis requires the traditional Bagnold scaling of the stresses (i.e. $p, \tau \sim \dot{\gamma}^2$), thereby rendering the intermediate and quasi-static regimes impossible. This picture is consistent with the vanishing of the intermediate regime observed in Figure 2 as $k \rightarrow \infty$. However, real granular materials do nevertheless have a finite stiffness. Therefore, in the context of building a

general rheological model for granular flows, it is preferable to choose a framework that include all three regimes.

Another important observation from Figure 2 is the smoothness of the transitions between the regimes. This feature suggests that purely quasi-static, inertial, or intermediate flow is achieved only in certain limits. As $\hat{\gamma} \rightarrow 0$, we see quasi-static flow for $\phi > \phi_c$, inertial flow for $\phi < \phi_c$, and intermediate flow at $\phi = \phi_c$. We also see intermediate flow as $\hat{\gamma} \rightarrow \infty$ for all volume fractions over the wide range examined in this study. The smooth transitions also suggest that the rheology at a particular $(\dot{\gamma}, \phi)$ is a composite of contributions from low- $\hat{\gamma}$ and high- $\hat{\gamma}$ behaviors, and this notion will play a large role in our construction of a rheological model.

IV. CRITICAL VOLUME FRACTION ϕ_c

Because ϕ_c plays such an important role in governing the rheology in each of the three flow regimes, accurate estimation of its value for each case of μ is required for the construction of a valid rheological model. However, this task is made difficult by fluctuations of our measurements in time t . We observe a propensity for assemblies near ϕ_c to form and break force chains intermittently during the shearing process, resulting in stress fluctuations of several orders of magnitude as seen in Figure 3a. Though fluctuations occur at all volume fractions, their size relative to the mean is markedly large near the critical point. In Figure 3b the standard deviation $\sigma_p \equiv \sqrt{\langle p^2(t) \rangle - \langle p(t) \rangle^2}$ of the pressure, when scaled by the time-averaged pressure p , exhibits a spike centered slightly under ϕ_c . This phenomenon increases the potential error in the time-averaged stress values near the critical point, thereby limiting the precision of our ϕ_c estimates to within about ± 0.001 .

Additionally, though ϕ_c is certainly an important quantity, it is not necessarily the only or even the most influential parameter describing the jamming transition. The fact that stress can vary significantly at a constant volume fraction indicates that, while ϕ is a useful predictor of time-averaged stresses, other state variables may be more suitable for predicting instantaneous stresses. This quality has been observed previously with the coordination number $Z(t)$, for example, which was shown to exhibit a one-to-one correspondence with $p(t)$ in the quasi-static regime [23]. Indeed, we observe that $p(t)$ and $Z(t)$ exhibit the same qualitative evolution in time (Figure 3c) and a similar ϕ -dependence in their fluctuations (Figure 3d). Here we define $Z(t) \equiv 2N_c(t)/N$ for N_c contacts occurring in the N -particle assembly. The $p(t)$ - $Z(t)$ relationship suggests that the critical point is better defined by some critical coordination number Z_c . However, because our goal is the construction of a *steady-state* rheological model, it is convenient to ignore all dynamics and assume that Z_c and ϕ_c correspond to the same conditions. We therefore proceed with ϕ_c as the definition of the critical point for our model.

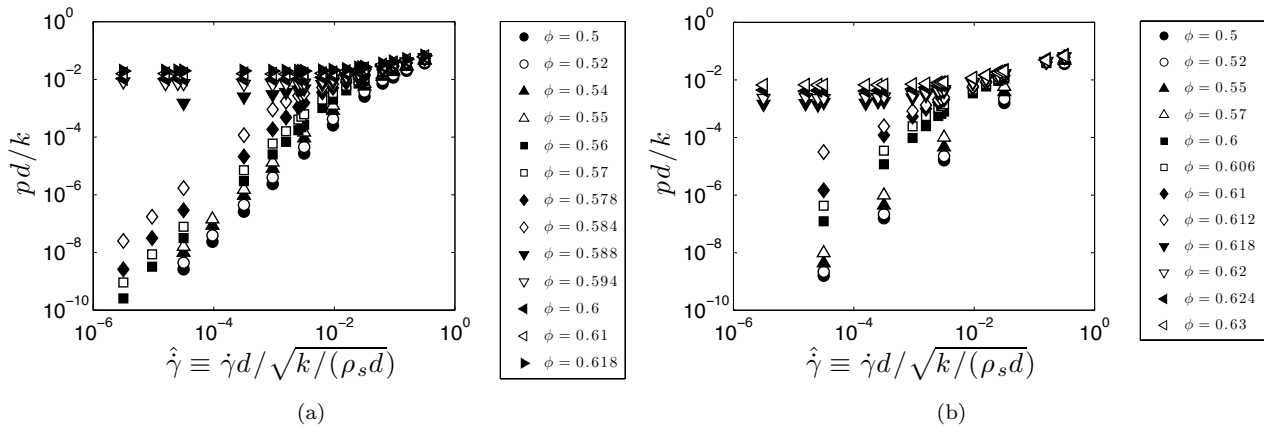


FIG. 1. Dimensionless pressure vs. dimensionless shear rate for various volume fractions with (a) $\mu = 0.5$ and (b) $\mu = 0.1$. In both cases, three flow regimes are observed, each with the scalings $p \sim \hat{\gamma}^m$: a quasi-static regime with $m = 0$, an inertial regime with $m = 2$, and an intermediate regime with $m \approx 1/2$. At low $\hat{\gamma}$, a critical volume fraction ϕ_c separates the quasi-static and inertial regimes; values of $\phi_c(\mu)$ are given in Table I.

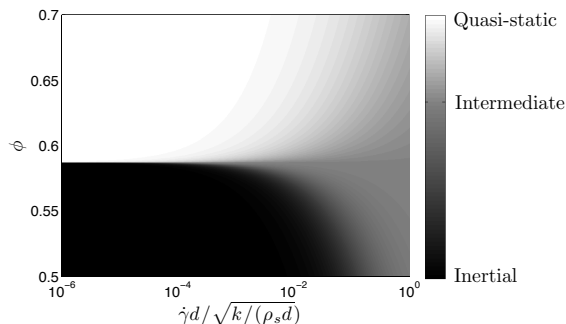


FIG. 2. Regime map for $\mu = 0.5$, with volume fraction vs. dimensionless shear rate. The intermediate regime occurs only at ϕ_c in the limit $\hat{\gamma} \rightarrow 0$ but emerges from this point to encompass all volume fractions as $\hat{\gamma} \rightarrow \infty$.

In addition to being a function of μ , the critical point has also been proposed to change with the restitution coefficient e [24], and such a $\phi_c(e)$ has been used in a kinetic theory for frictional particles [25]. However, our DEM results do not support this conclusion, especially for frictional particles. As seen in Figure 4a-b for $\mu = 0.5$ and $\mu = 0.1$, the spike in the pressure fluctuations occurs at the same volume fraction for a given μ regardless of the value of e , suggesting that $\phi_c = \phi_c(\mu)$ only. Even for the frictionless case (Figure 4c), where fluctuations tend to occur over a wider range of volume fractions, there is no clear trend in the peak towards lower ϕ . One possible reason for the discrepancy is the methods used for determining ϕ_c . Because hard-sphere codes, used in Ref. [24], prohibit particle overlaps, they are unable to simulate sheared particle systems near or above ϕ_c [26]. This shortcoming limits the performable simulations to one side of ϕ_c , thus requiring the critical point to be estimated via extrapolation. Furthermore, while hard-

sphere methods treat collisions as binary interactions, entrance into the quasi-static regime coincides with the development of multi-body interactions that persist even in the hard-sphere limit [27]. This conflict may render even-driven algorithms less accurate at resolving collisions upon approaching ϕ_c and perhaps result in an erroneous estimation of the value of ϕ_c . Soft-sphere DEM, on the other hand, enables us to resolve multi-body contacts and simulate shear flows at any volume fraction on either side of ϕ_c , thereby allowing us to *interpolate* the value of ϕ_c . For these reasons, we expect the latter approach to provide more accurate ϕ_c estimates.

V. PRESSURE SCALINGS AND REGIME BLENDING

It has been demonstrated in experimental [10] and computational [8, 9, 12] studies of frictionless particles that stress data will collapse onto two curves (one above ϕ_c and one below) upon scaling the stresses and shear rate by powers of $|\phi - \phi_c|$, the distance to jamming. This idea is consistent with several models of the radial distribution function, used in kinetic theories for the inertial regime, that diverge at close packing [28–30]. Such a collapse can be achieved for frictional particles as well, as shown in Figure 5, with

$$p^* = p/|\phi - \phi_c|^a \quad \dot{\gamma}_p^* = \dot{\gamma}/|\phi - \phi_c|^b \quad (4)$$

and constitutive exponents a and b . This result for frictional disks was also found independently in Ref. [15]. From the collapse it is clear that an asymptotic power-law relationship between stress and shear rate exists for each flow regime j , and we can write the form of each asymptote as

$$\frac{p_j}{|\phi - \phi_c|^a} \sim \left[\frac{\dot{\gamma}}{|\phi - \phi_c|^b} \right]^{m_j} \quad (5)$$

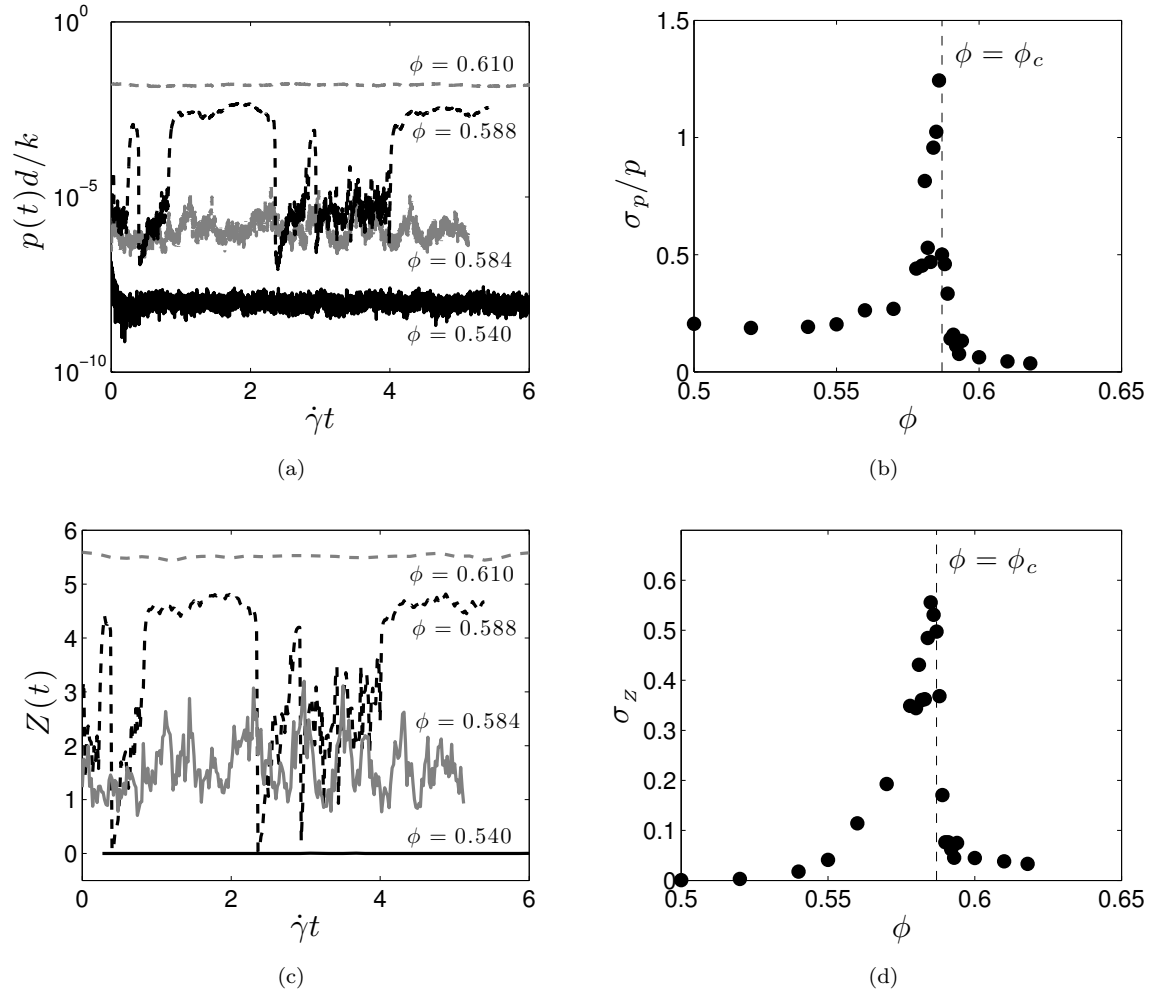


FIG. 3. Characteristics of the critical point for $\mu = 0.5$ and $\hat{\gamma} = 3.2 \times 10^{-5}$. (a) Pressure fluctuations in time are observed to become larger near the critical point. (b) The standard deviation of pressure, scaled by the mean pressure, exhibits a spike at ϕ_c . (c-d) The coordination number fluctuations are similar to those of the pressure in terms of both dynamics and ϕ -dependence.

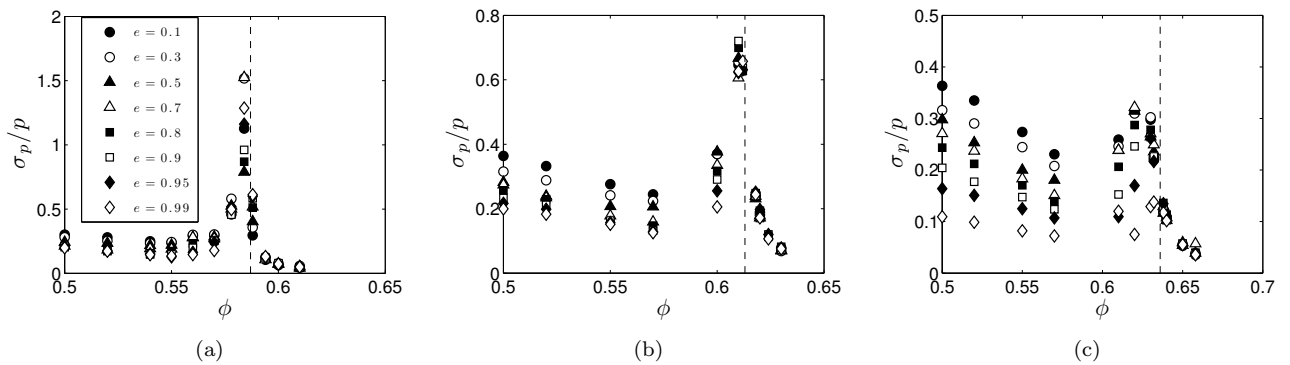


FIG. 4. Effect of changing the restitution coefficient on the pressure fluctuations for $\hat{\gamma} = 3.2 \times 10^{-5}$. Dotted lines demarcate the critical point ϕ_c . For (a) $\mu = 0.5$ and (b) $\mu = 0.1$, the location of the spike in pressure fluctuations is independent of e . (c) Even for the frictionless case, there is little evidence to suggest $\phi_c = \phi_c(e)$.

where $m_{\text{QS}} = 0$, $m_{\text{Inert}} = 2$, and $m_{\text{Int}} = m^*$. The exponents a and b can be fitted from the DEM data, but the values are sensitive to the choice of ϕ_c used [9] and hence should be chosen with care. Our inertial regime data suggest that $p_{\text{Inert}} \sim |\phi - \phi_c|^{-2}$, which is consistent with previous results [31]; quasi-static regime data reveal that $p_{\text{QS}} \sim |\phi - \phi_c|^{2/3}$; and, as noted earlier, $p_{\text{Int}} \sim |\phi - \phi_c|^0$. These trends lead us to set $a = 2/3$, $b = 4/3$, and $m^* = 1/2$. The m^* value is consistent with our fits of the intermediate asymptote (Table I) and with experimental results [10, 11], and it is similar to other values proposed for frictionless particles using the linear spring-dashpot model [8, 9]. The value of a used in Ref. [23] ($a = 1$), though different, still yields a decent collapse. However, in that work, ϕ_c is determined by extrapolation from the quasi-static regime, while here we interpolate it from quasi-static and inertial regime data and furthermore verify it with stress fluctuation data, as described in Section IV; hence we believe our current ϕ_c values and the resulting a value to be more accurate. We also point out that the above scaling exponents depend on the contact model used [8, 32]. Based on a small set of simple shear simulations with a Hertzian contact model, we observe the values of $a \approx 1$ and $m^* \approx 3/4$ to be larger than in the LSD case by a factor of 3/2, which is consistent with previous results for static, jammed systems [16]. The value of b , however, remains the same for both contact models; note that in both cases $a = bm^*$ in order to satisfy the functional forms implied by the collapse. The resulting collapse for the Hertzian particles is shown in Figure 6.

Though the individual regime limits can be described using Eq. 5, the transitions between them have yet to be modeled. To this end, we employ a blending function B of the form

$$B(y_1, y_2) = (y_1^w + y_2^w)^{1/w} \quad (6)$$

with $w > 0$ yielding an additive blend for the quasi-static-to-intermediate transition and $w < 0$ providing a harmonic blend for the inertial-to-intermediate transition. Figure 5 demonstrates the use of Eq. 6 with the asymptotic forms of Eq. 5 and $w = \pm 1$. The blended model is able to capture the pressure behavior continuously in shear rate for all three regime limits as well as the transitions; moreover, it does so without defining the stresses in piecewise fashion over arbitrary shear rate domains. Notably, it also predicts the narrowing intermediate window around $\phi = \phi_c$ in the limit of zero shear rate, as the quasi-static and inertial contributions to the stress become small near the jamming point. The general form of the pressure model based on the Hookean-case results can hence be written as

$$p = \begin{cases} p_{\text{QS}} + p_{\text{Int}} & \text{for } \phi \geq \phi_c \\ (p_{\text{Inert}}^{-1} + p_{\text{Int}}^{-1})^{-1} & \text{for } \phi < \phi_c \end{cases} \quad (7)$$

TABLE II. Values of model constants

μ -dependent parameters							
μ	0.0	0.1	0.3	0.5	1.0		
η_s	0.105	0.268	0.357	0.382	0.405		
α_{QS}	0.095	0.083	0.14	0.20	0.25		
μ -independent parameters							
α_{Inert}	α_{Int}	I_0	α_1	β_1	$\hat{\gamma}_0$	α_2	β_2
0.021	0.099	0.32	0.37	1.5	0.1	0.2	1.0

with the individual regime contributions defined as

$$p_{\text{QS}}d/k = \alpha_{\text{QS}}|\phi - \phi_c|^{2/3} \quad (8)$$

$$p_{\text{Int}}d/k = \alpha_{\text{Int}}\hat{\gamma}^{1/2} \quad (9)$$

$$p_{\text{Inert}}d/k = \frac{\alpha_{\text{Inert}}\hat{\gamma}^2}{|\phi - \phi_c|^2}. \quad (10)$$

The pressure at $\phi = \phi_c$ can be calculated using either blend, since Eqs. 8 and 10 yield $p_{\text{QS}}(\phi = \phi_c) = 0$ and $p_{\text{Inert}}(\phi = \phi_c) = \infty$, which both yield $p = p_{\text{Int}}$ upon substitution into Eq. 7; this case is included with the quasi-static blending solely for the sake of simplicity. The constitutive parameter α_{QS} is a function of μ , while α_{Inert} and α_{Int} are fairly μ -independent. These and other model constants are given in Table II.

There are a few features of Eqs. 7- 10 that are worth noting. Firstly, for systems above the critical volume fraction, the blending function yields a model of Herschel-Bulkley form, which has been shown previously to capture the shear stress of soft-sphere systems [10, 11]. Additionally, the individual regime contributions are consistent with some known scalings. For example, the quasi-static pressure is proportional to the particle stiffness [23], while $p_{\text{Inert}} = \alpha_{\text{Inert}}\rho_s(\hat{\gamma}d)^2/|\phi - \phi_c|^2$ rightly exhibits no dependence on k [1-4]. Finally, the viability of the ϕ -scaling in Eq. 10 for all μ values suggests that the $\phi_c = \phi_c(\mu)$ formulation could be a simple but effective step in improving current kinetic theory models.

VI. DIMENSIONLESS GROUPS AND STRESS RATIO MODEL

It is possible to construct an analogous model for the shear stress as for the pressure, as previous works have shown τ to exhibit similar scalings with respect to the distance to jamming [8, 9, 13]. However, because τ and p both vary over several orders of magnitude, fitting them directly can result in poor predictions of their ratio, *i.e.* the shear stress ratio $\eta \equiv \tau/p$, which varies over a much narrower range. For this reason, we choose to construct a model for η and then express the shear stress as $\tau = \eta p$.

Some recent, successful rheological models for dense granular flows employ a dimensionless parameter called the inertial number as the basis for achieving stress collapses over a range of volume fractions and shear rates

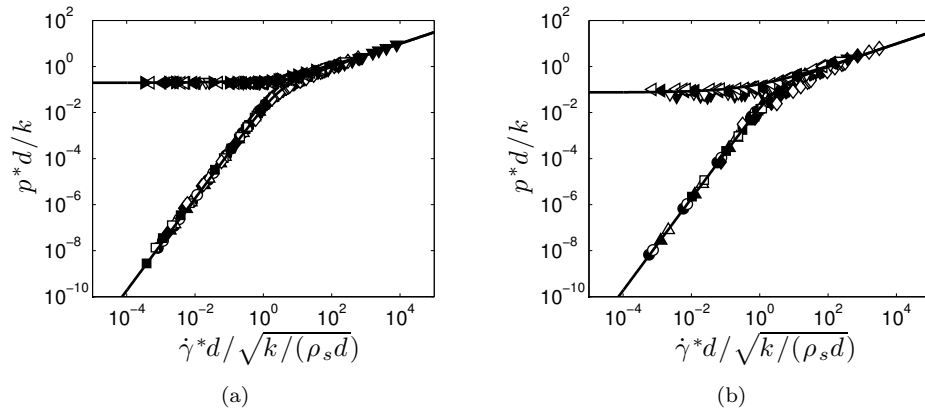


FIG. 5. Collapse of pressure vs. shear rate curves from Figure 1 for (a) $\mu = 0.5$ and (b) $\mu = 0.1$. In both cases, the pressure is scaled as $p^* = p/|\phi - \phi_c|^{2/3}$ and the shear rate as $\dot{\gamma}^* = \dot{\gamma}/|\phi - \phi_c|^{4/3}$. A simple blending function (solid lines) captures regime asymptotes and transitions.

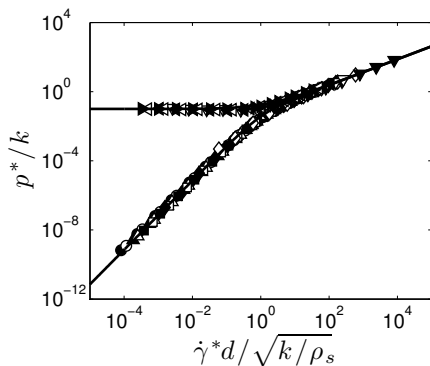


FIG. 6. Collapse of pressure vs. shear rate curves for Hertzian particles with $\mu = 0.5$. The volume fractions (and legend) are the same as from Figure 1(a). Here, $p^* = p/|\phi - \phi_c|^1$, $\dot{\gamma}^* = \dot{\gamma}/|\phi - \phi_c|^{4/3}$, and $m^* \approx 3/4$. Regime asymptotes and transitions are captured by the same blending function (solid lines) as in the Hookean case.

[31, 33, 34]. This inertial number $I \equiv \dot{\gamma}d/\sqrt{p/\rho_s}$ is a ratio of the timescales of shear deformation and particle rearrangement, and the physics of granular flows of hard particles is said to be determined by the competition of these two mechanisms. When the particles have a finite stiffness, however, the binary collision time is nonzero and therefore presents yet another important timescale. With this point in mind, we note that the dimensionless shear rate $\hat{\gamma}$ identified earlier is in fact the ratio of the binary collision time to the macroscopic deformation time [14], and we show here that it can be used along with the inertial number to characterize soft particle rheology.

In Figure 7 we plot the stress ratio versus the inertial number for $\mu = 0.5$. For the densest systems, *i.e.* for low I , η exhibits a constant-value asymptote that we identify as the yield stress ratio $\eta_s = \eta_s(\mu)$; values of η_s for different cases of μ are presented in Table II. As

I increases, η then also increases. These same observations were made in previous studies of particles in the infinitely-hard limit [31, 33, 34]. However, unlike in these works, we also observe significant scatter as I becomes larger, which we will now show to be a consequence of the particle softness.

Because the inertial number models are designed for hard particles, we first limit our analysis to cases in which particle softness has little effect, *i.e.* for small $\hat{\gamma}$. Indeed, quasi-static and inertial regime data of η versus I from our DEM simulations collapse onto a single curve, with the quasi-static regime occurring for $I \lesssim 10^{-2}$ and inertial regimes occurring for $I \gtrsim 10^{-2}$. This collapse is seen in the inset of Figure 7a for $\mu = 0.5$. We model this curve as

$$\eta_{\text{hard}}(I) = \eta_s(\mu) + \frac{\alpha_1}{(I_0/I)^{\beta_1} + 1}, \quad (11)$$

where I_0 , α_1 , and β_1 are parameters dictating the transition from quasi-static to inertial flow. This form is similar to that of Jop *et al.* [34]. Interestingly, the increase of η from η_s is nearly identical for all cases of $\mu \geq 0.1$ (Fig. 7b). Since the interparticle friction coefficient for most real granular materials falls in this range, we conveniently take one set of constitutive parameter values as suitable averages for our model; these values are presented in Table II.

The form of η_{hard} presented in Eq. 11 is not the only viable option. Another possibility is a simple power law, which can be written as $\eta_{\text{hard}}(I) = \eta_s + \alpha'_1 I^{\beta'_1}$. This form has been used previously by da Cruz and coworkers [31] with $\beta'_1 = 1$. A comparison between this form, with $\beta'_1 = 1$ and $\alpha'_1 = 0.6$, and the one in Eq. 11 are shown in Figure 7b. The two models agree closely for all values of $I \lesssim 0.3$, with a departure occurring for larger I . However, with the inertial number models, we need to be concerned only with volume fractions greater than the freezing transition $\phi_f = 0.49$ [28], where traditional kinetic theories fail [25, 35]. At ϕ_f , the kinetic theory

of Garzò and Dufty [1] predicts $I = 0.83$, which is consistent with our DEM results and beyond which we can ignore disparities in the η_{hard} predictions between the two models. Hence, though we continue with Eq. 11, we view both forms as being acceptable.

Though Eq. 11 captures low- $\hat{\gamma}$ behavior well, inclusion of higher- $\hat{\gamma}$ cases reveals a noticeable departure from the $\eta_{\text{hard}}(I)$ curve, as seen in Figure 7. Specifically, for a given value of I , the value of η from an intermediate-regime flow is consistently lower than that given by the Eq. 11. This deviation is a consequence of particle softness and, in the context of our regime blending, grows in magnitude with the intermediate-regime contribution to the pressure. Figure 8a shows the connection between the magnitude of this departure $\eta_{\text{soft}} \equiv \eta_{\text{hard}} - \eta$ and $\hat{\gamma}$. This softness effect, similarly to η_{hard} , can be modeled as

$$\eta_{\text{soft}}(\hat{\gamma}) = \frac{\alpha_2}{(\hat{\gamma}_0/\hat{\gamma})^{\beta_2} + 1}, \quad (12)$$

where $\hat{\gamma}_0 = 0.1$, $\alpha_2 = 0.2$, and $\beta_2 = 1$ are constants describing the transition to intermediate flow. Finally, we can write

$$\eta(I, \hat{\gamma}) = \eta_{\text{hard}}(I) - \eta_{\text{soft}}(\hat{\gamma}), \quad (13)$$

and, by plotting $\eta^* \equiv \eta - \eta_s + \eta_{\text{soft}}$ vs. I as in Figure 8b, we arrive at a collapse of the stress ratio data from all three regimes.

VII. GENERALIZED CONTINUUM MODEL

Our rheological model therefore consists of Eqs. 7 - 10 for the pressure and Eqs. 11 - 13 for the shear stress ratio. Though the collapses can generally be improved by allowing the fitting parameters to be functions of μ rather than constants, the fits are nevertheless fairly good and hence justify the use of simpler forms.

While this model was developed for simple shear flows, it can be recast to handle general deformation types as done in Ref. [23]. First, we note that the strain rate tensor for simple shear flows is $\mathbf{D} = \frac{1}{2}\hat{\gamma}(\mathbf{e}_x\mathbf{e}_z + \mathbf{e}_z\mathbf{e}_x)$ where \mathbf{e}_i are the unit vectors in the i direction. This expression can be rearranged to yield

$$\hat{\gamma} = 2|\mathbf{D}|, \quad (14)$$

where $|\mathbf{D}| = \sqrt{\frac{1}{2}\mathbf{D}^{\mathbf{T}} : \mathbf{D}}$ is the modulus of \mathbf{D} , and \mathbf{D} is taken to correspond to general deformation types. Finally, we write the stress tensor as

$$\boldsymbol{\sigma} = p(\mathbf{I} - \eta\hat{\mathbf{S}}) \quad (15)$$

where p and η are given by our model, \mathbf{I} is the identity tensor, and $\hat{\mathbf{S}} = \mathbf{S}/|\mathbf{D}|$ with $\mathbf{S} = \mathbf{D} - \frac{1}{3}\text{tr}(\mathbf{D})$. Eqs. 14 and 15 allow our rheological model to handle flows in more complex geometries as are commonly found in real flow scenarios.

VIII. SUMMARY

We have investigated shear flows of dense frictional granular materials in all three flow regimes in order to gain a better understanding of the scalings within each regime and the transitions between them. We find scaling relations for the pressure with respect to both shear rate and the distance to the jamming point and, for the intermediate regime, observe identical power-law behavior for particles with different friction coefficients. Furthermore, we propose a simple blending function for patching each regime's asymptotic form in order to predict pressure in between regimes. Finally, we decompose the shear stress ratio into contributions from two dimensionless shear rates, enabling us to quantify the effect of particle softness. These findings establish a framework for a global model for steady-state simple shear flows of dense granular matter.

We gratefully acknowledge the support of DOE/NETL Grant No. DE-FG26-07NT43070.

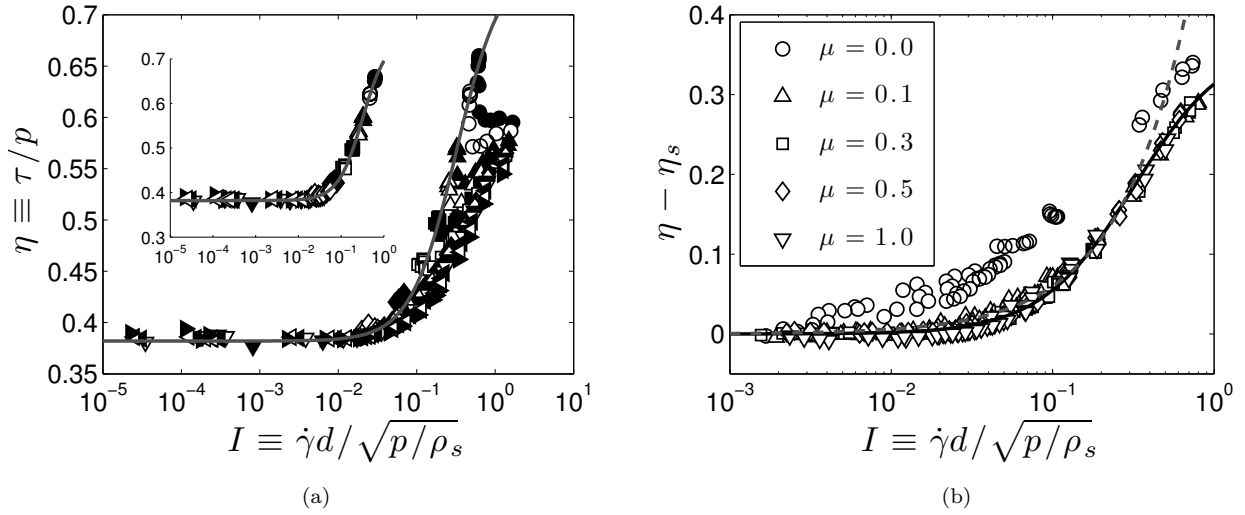


FIG. 7. Behavior of the shear stress ratio with respect to inertial number. (a) Significant scatter is observed when data from all three regimes are included. Data are shown for $\mu = 0.5$ (see legend in Figure 1a). Inset: A good collapse is achieved, however, for cases in which $\hat{\gamma} \leq 3.2 \times 10^{-5}$. These cases correspond essentially to the quasi-static ($I \lesssim 10^{-2}$) and inertial regimes ($I \gtrsim 10^{-2}$) and are also indicated with a best-fit line (Eq. 11) in the main figure. Intermediate regime data lie below this line. (b) The increase in the stress ratio from the yield stress ratio for these small- $\hat{\gamma}$ cases collapses for $\mu \geq 0.1$. Eq. 11 captures these data well (solid line), as does the model of da Cruz et al. [31] for $I \lesssim 0.3$ (dashed line).

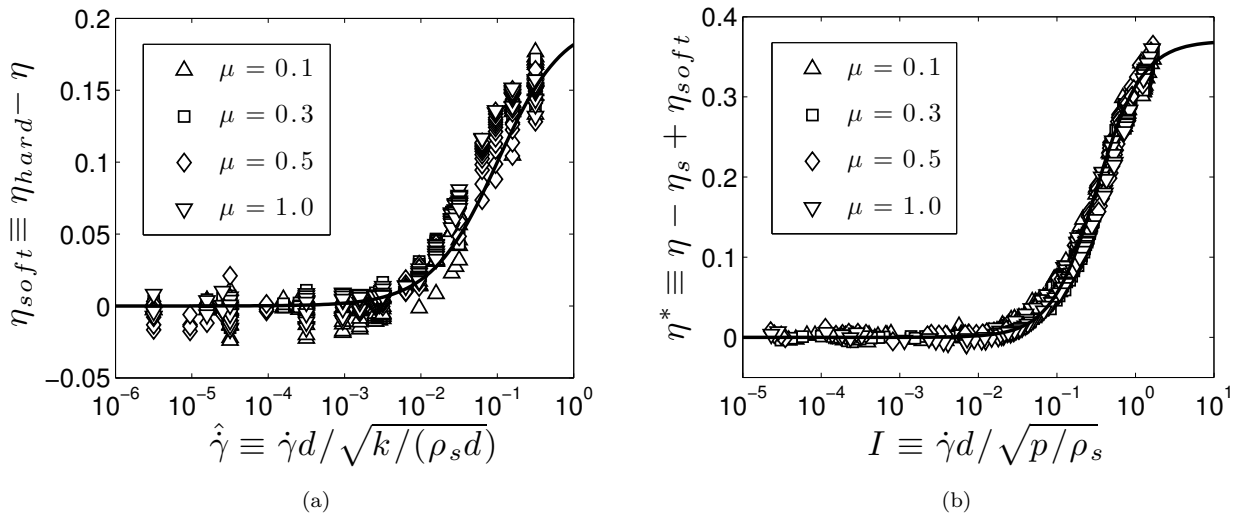


FIG. 8. Shear stress ratio contribution from $\hat{\gamma}$ for all values of $\hat{\gamma}$ and $\mu \geq 0.1$. (a) The softness-induced departure η_{soft} of the stress ratio from its hard-particle limit is essentially a function of only $\hat{\gamma}$. (b) The correction for particle softness yields a collapse of the data in all three regimes.

-
- [1] V. Garzó and J. W. Dufty, Phys. Rev. E **59**, 5895 (1999).
- [2] C. K. K. Lun, S. B. Savage, D. J. Jeffrey, and N. Chepurniy, J. Fluid Mech. **140**, 223 (1984).
- [3] J. T. Jenkins and M. W. Richman, Phys. Fluids **28**, 3485 (1985).
- [4] P. C. Johnson and R. Jackson, J. Fluid Mech. **176**, 67 (1987).
- [5] D. G. Schaeffer, J. Differ. Equations **66**, 19 (1987).
- [6] J. H. Prevost, Soil Dyn. Earthq. Eng. **4**, 9 (1985).
- [7] A. J. Liu and S. R. Nagel, Nature **396**, 21 (1998).
- [8] T. Hatano, J. Phys. Soc. Jpn. **77**, 123002 (2008).
- [9] M. Otsuki and H. Hayakawa, Phys. Rev. E **80**, 011308 (2009).
- [10] K. N. Nordstrom, E. Verneuil, P. E. Arratia, A. Basu, Z. Zhang, A. G. Yodh, J. P. Gollub, and D. J. Durian, Phys. Rev. Lett. **105**, 175701 (2010).
- [11] J. R. Seth, M. Cloitre, and R. T. Bonnecaze, **52**, 1241 (2008).
- [12] P. Olsson and S. Teitel, Phys. Rev. Lett. **99**, 178001 (2007).
- [13] B. P. Tighe, E. Woldhuis, J. J. C. Remmers, W. van Saarloos, and M. van Hecke, Phys. Rev. Lett. **105**, 088303 (2010).
- [14] C. S. Campbell, J. Fluid Mech. **465**, 261 (2002).
- [15] M. Otsuki and H. Hayakawa, Phys. Rev. E **83**, 051301 (2011).
- [16] H. P. Zhang and H. A. Makse, Phys. Rev. E **72**, 011301 (2005).
- [17] C. Song, P. Wang, and H. A. Makse, Nature **453**, 629 (2008).
- [18] T. S. Majmudar, M. Sperl, S. Luding, and R. P. Behringer, Phys. Rev. Lett. **98**, 058001 (2007).
- [19] M. van Hecke, J. Phys. Condens. Mat. **22**, 033101 (2010).
- [20] P. A. Cundall and O. D. L. Strack, Geotechnique **29**, 47 (1979).
- [21] S. Plimpton, J. Comput. Phys. **117**, 1 (1995).
- [22] A. W. Lees and S. F. Edwards, J. Phys. C **5**, 1921 (1972).
- [23] J. Sun and S. Sundaresan, Journal of Fluid Mechanics **682**, 590 (2011).
- [24] V. Kumaran, Journal of Fluid Mechanics **632**, 109 (2009).
- [25] J. Jenkins and D. Berzi, Granular Matter **12**, 151 (2010).
- [26] T. Pöschel and T. Schwager, *Computational Granular Dynamics: Models and Algorithms* (Springer, Berlin, 2005).
- [27] N. Mitarai and H. Nakanishi, Phys. Rev. E **67**, 021301 (2003).
- [28] S. Torquato, Phys. Rev. E **51**, 3170 (1995).
- [29] C. Lun and S. Savage, Acta Mechanica **63**, 15 (1986).
- [30] S. Ogawa, A. Umemura, and N. Oshima, Z. Angew. Math. Phys. **31**, 483 (1980).
- [31] F. da Cruz, S. Emam, M. Prochnow, J.-N. Roux, and F. Chevoir, Phys. Rev. E **72**, 021309 (2005).
- [32] M. Otsuki and H. Hayakawa, Prog. Theor. Phys. **121**, 647 (2009).
- [33] G. MiDi, Eur. Phys. J. E **14**, 341 (2004).
- [34] P. Jop, Y. Forterre, and O. Pouliquen, Nature **441**, 727 (2006).
- [35] Y. Forterre and O. Pouliquen, Annu. Rev. Fluid Mech. **40**, 1 (2008).